

Article

# Controllable Preparation of SERS-Active Ag-FeS Substrates by a Cosputtering Technique

Ning Ma <sup>1</sup>, Xin-Yuan Zhang <sup>2</sup>, Wenyue Fan <sup>1</sup>, Bingbing Han <sup>1</sup>, Sila Jin <sup>3</sup>, Yeonju Park <sup>3</sup>,  
Lei Chen <sup>1,\*</sup>, Yongjun Zhang <sup>2,\*</sup>, Yang Liu <sup>2</sup>, Jinghai Yang <sup>2</sup> and Young Mee Jung <sup>3,\*</sup> 

<sup>1</sup> Key Laboratory of Preparation and Applications of Environmental Friendly Materials, Ministry of Education, College of Chemistry, Jilin Normal University, Changchun 130103, China; elva\_maning@163.com (N.M.); 15504341371@163.com (W.F.); bingbinghan0106@163.com (B.H.)

<sup>2</sup> Key Laboratory of Functional Materials Physics and Chemistry, Ministry of Education, College of Physics, Jilin Normal University, Changchun 130103, China; zxycomp@126.com (X.-Y.Z.); liuyang@jlnu.edu.cn (Y.L.); jhyang1@jlnu.edu.cn (J.Y.)

<sup>3</sup> Department of Chemistry, Institute for Molecular Science and Fusion Technology, Kangwon National University, Chunchon 24341, Korea; jsira@kangwon.ac.kr (S.J.); yeonju4453@kangwon.ac.kr (Y.P.)

\* Correspondence: chenlei@jlnu.edu.cn (L.C.); yjzhang@jlnu.edu.cn (Y.Z.); ymjung@kangwon.ac.kr (Y.M.J.); Tel.: +82-33-250-8495 (Y.M.J.)

Academic Editor: Keith C. Gordon

Received: 10 December 2018; Accepted: 29 January 2019; Published: 2 February 2019



**Abstract:** In this work, we introduced an ordered metal-semiconductor molecular system and studied the resulting surface-enhanced Raman scattering (SERS) effect. Ag-FeS nanocaps with sputtered films of different thicknesses were obtained by changing the sputtering power of FeS while the sputtering power of Ag and the deposition time remained constant. When metallic Ag and the semiconductor FeS are cosputtered, the Ag film separates into Ag islands partially covered by FeS and strong coupling occurs among the Ag islands isolated by FeS, which contributes to the SERS phenomenon. We also investigated the SERS enhancement mechanism by decorating the nanocap arrays produced with different FeS sputtering powers with methylene blue (MB) probe molecules. As the FeS sputtering power increased, the SERS signal first increased and then decreased. The experimental results show that the SERS enhancement can mainly be attributed to the surface plasmon resonance (SPR) of the Ag nanoparticles. The coupling between FeS and Ag and the SPR displacement of Ag vary with different sputtering powers, resulting in changes in the intensity of the SERS spectra. These results demonstrate the high sensitivity of SERS substrates consisting of Ag-FeS nanocap arrays.

**Keywords:** PSCP templates; cosputtering; SERS; SPR

## 1. Introduction

In 1974, Fleischmann and his collaborators found for the first time that pyridine on the surface of a rough silver electrode generates a strong Raman signal [1]. The unique advantages of surface-enhanced Raman scattering (SERS) perfectly solve the shortcomings of weak Raman signal strengths and this technique is thus widely used in surface and interface analysis, chemistry, catalysis, biosensing, medical detection and trace analysis [2–4]. At present, studies of the nature of the SERS enhancement mechanism are based on the enhancement of the incident electric field,  $E$  and the change in the molecular polarizability,  $\alpha$ , which correspond to an electromagnetic field enhancement mechanism (EM) [5,6] and a chemical enhancement mechanism (CM) [7,8]. According to classical electromagnetic theory, the Raman scattering intensity is proportional to the square of the molecular dipole moment ( $p = \alpha R$ ). When the frequency of the incident light matches the natural frequency of the electronic

oscillation of the surface of the metal nanoparticles (NPs), the amplitude of the oscillation is maximized. This phenomenon is called localized surface plasmon resonance (LSPR) [9]. When an applied electromagnetic field is coupled with surface charge density oscillations, LSPR is excited at the interface between the metal nanofilm and the medium. The position of the LSPR peak is affected by the real part ( $\epsilon_1$ ) of the dielectric constant of the metal NP and the dielectric constant ( $\epsilon_m$ ) [10] of the surrounding medium, as well as the size and shape of the particle [11,12]. When a metal is combined with a semiconductor, a new LSPR mode is formed. Resonant coupling between metal NPs and between metal NPs and the semiconductor changes the optical properties. SERS is one of the most important applications of the LSPR effect. EM is an inherent property of metal NPs and is independent of the adsorbed molecules; CM is more complicated than EM. CM occurs via short-range chemical adsorption and is derived from the interactions between the metal substrate and the adsorbed molecules, which change the molecular polarizability [13–27]. The SERS effect is achieved by changing the polarizability of the new CT excited state formed by the interactions between the molecule and the substrate [19,28]. EM is generally considered to be much larger than CM but it is difficult to distinguish the two effects strictly by experimental means and the two mechanisms coexist in many systems.

Ag NPs are one of the most common metal materials used for Raman signal enhancement and they have been extensively studied in nanotechnology due to their unique optical properties and inherent SPR properties. However, since Ag is easily oxidized and biologically toxic, the use of this metal is limited [29]. The semiconductor FeS has specific electron-transfer capabilities and good adsorption characteristics as well as a narrow band gap. Optimized FeS shell-encapsulated NPs can be used as a stable SERS-active substrate to avoid the generation of background fluorescence and improve the SERS quality. A FeS layer also reduces the rate of Ag oxidation and increases the stability of the Ag NPs [30]. To date, the SERS mechanism for the interaction between ultranarrow-bandgap semiconductors and metals is still not fully understood. Therefore, designing and fabricating a Ag-FeS composite as a simple and controllable SERS enhancement substrate with semiconductor films of different thickness to regulate the metal SPR is of great importance. The microstructure and properties of nanocomposite film materials are closely related to the preparation process. The properties of the prepared films will be different by changing the substrate bias [31], deposition temperature [32], power or time [31], target composition [33] and  $N_2$  flow rate [34]. The microstructure and properties can be flexibly controlled by changing the parameters of cosputtering method. It is convenient to study the effects of different power and different sputtering time on the morphology and structure of the film and the effect of SPR on SERS performance.

In our work, a Ag-FeS nanocap array was fabricated by dual target cosputtering; the FeS sputtering power was changed while maintaining a constant deposition time and a constant sputtering power were used for Ag. Thus, Ag-FeS nanocaps with sputtered films of different thicknesses were obtained. The film deposition rate increased as the sputtering power of the FeS target increased. During sputter coating, the deposition rate is proportional to the rate at which atoms escape from the cathode target. In addition, the radio frequency (RF) sputtering power was increased, causing the majority of the sputtered particles to have high energy and these particles will have defects at the impact points. Since the combined energy of these defective regions is higher than that of the adjacent regions, defects are the preferred nucleation sites. Thus, increased sputtering power accelerates film growth and enhances the crystallinity of the resulting film. As the semiconductor FeS is introduced in a large amount in the system, the resulting layer will cover the surface of the Ag particle. At different sputtering powers, the coupling between FeS and Ag and the SPR displacement of Ag change, changing the intensity of the SERS spectra.

## 2. Results and Discussion

The Ag-FeS nanocap arrays were prepared by double-target cosputtering using colloidal sphere arrays of 200-nm polystyrene colloidal particles (PSCPs) as the substrate. The PSCP templates were assembled on silicon wafers by a self-assembly method. Figure 1 and Figure S1 show the high and low magnification SEM images of Ag-FeS nanocaps deposited on the PSCP template. These ordered colloidal sphere arrays have a tight, hexagonal symmetrical structure when Ag and FeS are cosputtered on a densely packed PSCP template, forming a rough Ag-FeS nanocap structure. Ag-FeS nanocaps with sputtered films of different thicknesses were obtained by changing the sputtering power of FeS while maintaining a constant deposition time and Ag sputtering power. When the FeS sputtering power was 50 W (Figure 1a), the surfaces of the Ag-FeS nanocaps are still smooth. As the sputtering power increases, small rough NPs appear in individual regions of the PSCP template. When the sputtering power is 80 W (Figure 1d), there are some higher cluster formations on the surfaces of the colloidal spheres; this morphology is due to the increase in FeS sputtering power, which ionizes more Ar into Ar<sup>+</sup>. The number of Fe NPs deposited on the substrate increases and the roughness is maximized. However, when the sputtering power is increased to 90 W, the surface of the sample is smoother due to the sputtered FeS particles and the cumulative agglomeration phenomenon is weakened. This morphological change is mainly due to nucleation and growth processes, as described by film formation and growth theory. The film deposition rate increases as the sputtering power of the FeS target increases. During sputter coating, the deposition rate is proportional to the rate at which atoms escape from the cathode target. In addition, the RF sputtering power is increased, so most of the sputtered particles have high energy and these particles will cause defects at the impact points. Since the combined energy of these defective regions is higher than that of the adjacent regions, the defects become the preferred nucleation sites and accelerated film growth and increase the crystallinity of the resulting film.

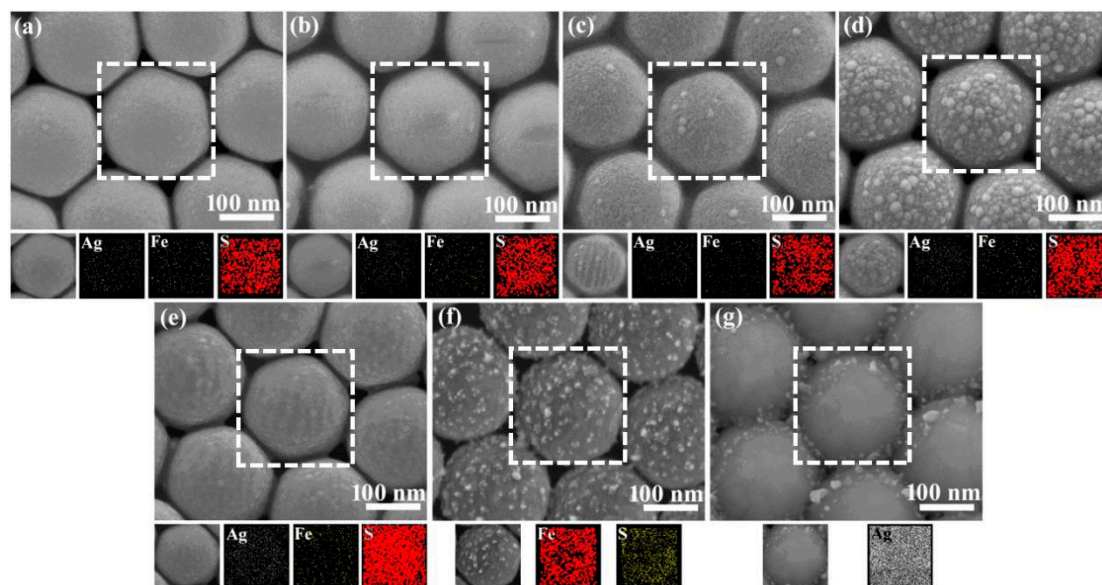


**Figure 1.** SEM images of the ordered Ag-FeS arrays, which were prepared by cosputtering Ag with a constant sputtering power (5 W) and FeS with varied sputtering powers for 300 s on the PSCP templates. The sputtering powers of FeS were (a) 50 W, (b) 60 W, (c) 70 W, (d) 80 W and (e) 90 W; sputtered pure FeS (f); and pure Ag (g) for 300 s.

The roughness of the base material influences the SPR. In the UV-Vis absorption spectra shown in Figure 2, the absorption peak at approximately 294 nm is attributed to the interband transition of silver [35]. The absorption peak located near 509 nm is attributed to the LSPR between the dipoles derived from the Ag/FeS array [36]. The EM interactions between the dipole and the particle are different, resulting in a change in the peak intensity. The Ag/FeS peaks shift because when the Ag and FeS are deposited, the electronic environment around the array was changed based on the interactions between Ag and FeS. The change in the SPR characteristics is caused by electron transfer [37]. The interparticle coupling is dominant and leads to a shift in the LSPR. As the content of Ag NPs increases, they accumulate on the surface of the base material together with FeS and the in-plane coupling increases, redshifting the LSPR. As the FeS content on the semiconductor increases, outer plane coupling occurs and the in-plane coupling decreases, blueshifting LSPR [38].

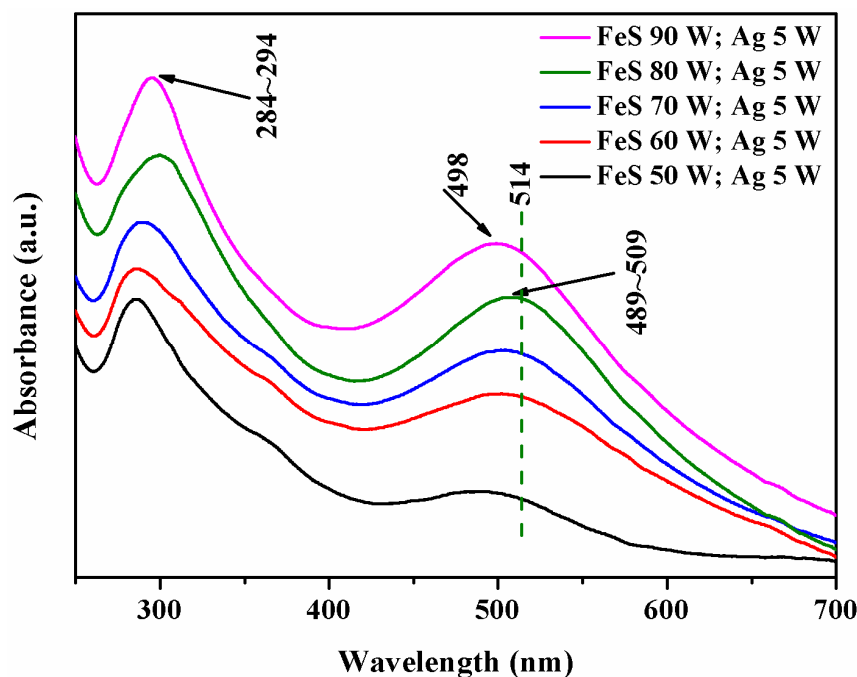


**Figure 2.** UV-Vis absorbance spectra of cosputtered Ag and FeS; Ag was deposited with a constant sputtering power (5 W) and FeS was deposited with varied sputtering powers (50 W, 60 W, 70 W, 80 W and 90 W) for 300 s on PSCP templates.

The XPS spectra used to determine the phase of the elements and the state of the chemical bonds are given in Figure 3. The peak position at which an offset occurred due to surface static was referenced to contaminant carbon ( $C 1s = 284.6$  eV). The peaks at 711.0 and 724.4 eV in the Fe 2p spectrum shown in Figure 3a are attributed to the presence of Fe-S bonds [39]; the peak at 161.2 eV in the S 2p spectrum shown in Figure 3b is attributed to the FeS characteristic peak of  $S^{2-}$ , the peak at 162.3 eV is attributed to  $FeS_2/FeS$  [40] and the peaks at 162.9, 163.3 and 163.4 eV correspond to polysulfide. The peaks at 164.5, 168.2 and 168.3 eV indicate the  $S 2p_{3/2}$  and  $S 2p_{1/2}$  orbits, respectively [28]. The peaks of Ag  $3d_{5/2}$  and  $3d_{3/2}$  appear at 367.9 and 373.9 eV, respectively, in Figure 3c. The presence of C, S, Fe and Ag was confirmed by the XPS full-scan spectrum shown in Figure 3d, indicating the successful preparation of the cosputtered substrate.

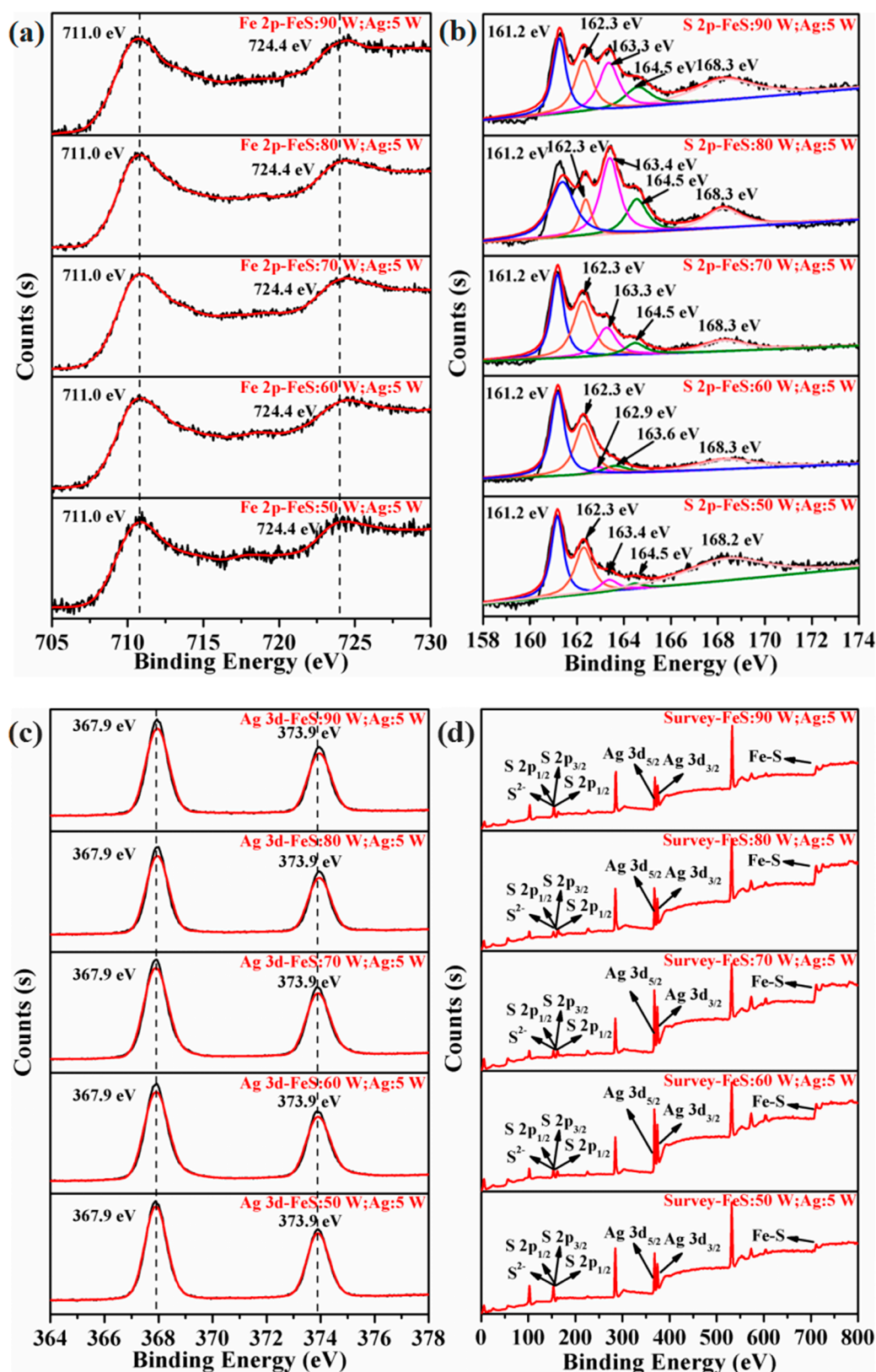


**Figure 3.** The XPS spectra of cosputtered Ag (5 W sputtering power) and FeS (50 W, 60 W, 70 W, 80 W and 90 W sputtering power) deposited for 300 s on the PSCP templates: Fe 2p (a), S 2p (b), Ag 3d (c) and survey (d) spectra.

To study the SERS activity of the Ag-FeS nanocap film, we chose MB as the probe molecule. Figure 4 shows the Raman spectrum of MB in ethanol; the characteristic Raman bands of MB at 445 and 1618  $\text{cm}^{-1}$  attributed to C–C stretching and C–N–C skeleton bending, respectively, can be observed [41] and characteristic bands of ethanol can be observed at 883 and 1067  $\text{cm}^{-1}$ . However, due to the low concentration, the characteristic MB bands are masked by the Raman scattering generated by the solvent and cannot be clearly observed.

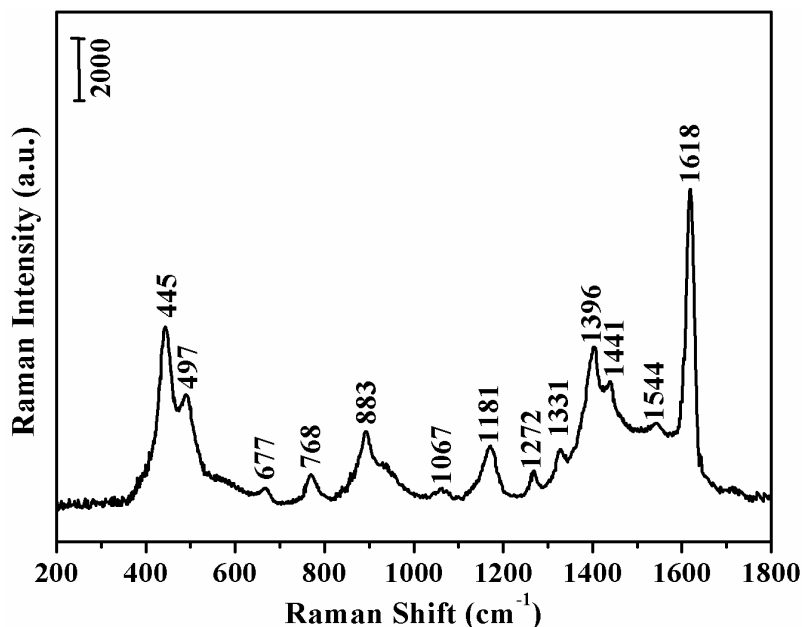
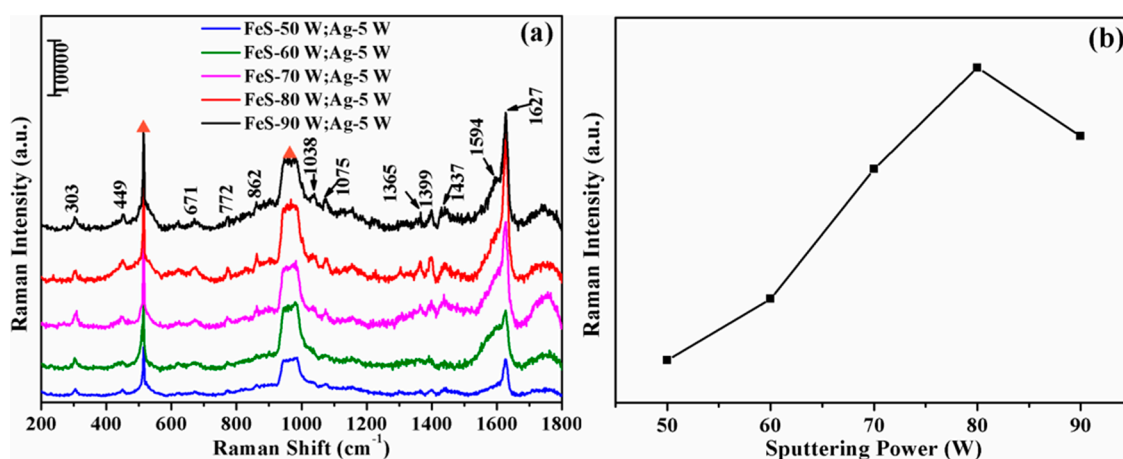


Figure 4. Raman spectrum of MB in ethanol.

Figure 5 shows the SERS spectra of MB adsorbed on the Ag-FeS module of the system at an excitation wavelength of 514 nm. The distribution of the SERS bands of MB is listed in Table 1 [38]. Compared with the Raman spectrum of MB in ethanol, some bands are better resolved in the SERS spectrum of the Ag-FeS-MB system but the characteristic bands of MB are clear. This distribution indicates that the molecules were well adsorbed onto the substrate material [41–43]. Furthermore, at an excitation wavelength of 514 nm, the band at 1618  $\text{cm}^{-1}$  splits into two bands at 1594 and 1627  $\text{cm}^{-1}$ . The displacement and splitting of some of the Raman bands indicates that the MB may be chemisorbed on the surface of the Ag-FeS nanocap film [44]. The peaks marked with triangles in the Figure 5a at 520 and 920–1000  $\text{cm}^{-1}$  are assigned to the Si peaks [45]. Figure 2 shows that the SPR absorption peak is closest to 514 nm at a FeS sputtering power of 80 W. Due to the resonance effect between the substrate and the laser at the excitation wavelength of 514 nm, the SERS spectrum of the substrate obtained with a FeS sputtering power of 80 W is the strongest, which consistent with the results of the UV-Vis spectra. We selected the characteristic MB band at 1627  $\text{cm}^{-1}$  and calculated the ratios of the Raman intensity as the sputtering power increased. When the FeS sputtering power is 80 W, the intensity of the MB signals reached their maximum. Based on the trend in the intensity of the band at 1627  $\text{cm}^{-1}$ , the maximum signal at 80 W is more intense than the corresponding signals obtained with other powers. An increase in power decreases the intensity of the signal due to the increased content of the semiconductor, which affects the electromagnetic field enhancement, so the SERS intensity gradually decreases after reaching the maximum value.



**Figure 5.** (a) SERS spectra of MB ( $10^{-3}$  mol/L) adsorbed on PSCP@Ag-FeS arrays with different FeS sputtering powers, the triangle-marked peaks were attributed to Si Wafer; (b) the ratios of the sputtering power of FeS to the Raman intensity of MB (taking  $1627\text{ cm}^{-1}$  as an example).

**Table 1.** Raman and SERS bands and band assignments of MB.

MB Raman Spectra	Excitation Wavelength (514 nm)	Band Assignments
445	449	$\delta$ (C–N–C)
497		$\delta$ (C–N–C)
677	671	$\nu$ (C–H)
768	772	
883	862	
	1038	$\beta$ (C–H)
1067	1075	
1181		$\nu$ (C–N)
1272		
1331	1365	
1396	1399	$\alpha$ (C–H)
1441	1437	$\nu_{\text{asym}}$ (C–N)
1544		$\nu_{\text{asym}}$ (C–C)
	1594	$\nu$ (C–C) ring
1618	1627	$\nu$ (C–C) ring

The intensities of the SERS signals are closely related to the size of the nanostructures, the surface roughness, the surrounding electrolyte environment and ‘hot spots.’ When Ag and FeS are cosputtered, the Ag film is separated into Ag islands partially covered by FeS and strong coupling occurs between the Ag islands isolated by FeS, which contributes to the SERS phenomenon. NPs optimized with semiconductor FeS shells can be used as a stable SERS-active substrate to avoid background fluorescence [46], which improves the quality of the SERS spectra. The deposited Ag film will gradually degrade and a FeS shell of the appropriate thickness as a metal deposition mask also reduces the rate of Ag oxidation, increases the stability of Ag and produces a greater SERS effect. However, as the distance from the surface of the metal to the outer surface of the FeS shell increases, the intensity of the electromagnetic field exponentially decrease and an excessively thick FeS shell will mask the surface plasmon band, which hinders the generation of SERS. The change in the SERS intensity of the Ag-FeS nanocap array is mainly due to the matching of the plasmon resonance peak with the excitation wavelength and the difference in the structural morphology. Therefore, sputtering FeS at different powers changes the surface roughness, making the plasma oscillation adjustable within a certain range and changing the SERS intensity. At an excitation wavelength of 514 nm, when Ag-FeS nanocap arrays are deposited on a 200-nm PSCP template, the sample prepared at a sputtering power

of 80 W has the largest surface roughness, which greatly increases the number of ‘hot spot’ regions, promoting the localization of electrons and significantly enhancing the SERS signal.

After obtaining the enhanced Raman signals of MB on the Ag/FeS array, we tried to estimate the surface enhancement factor on the array. The SERS enhancement factor (EF) is an important physical quantity for the quantitative comparison of substrate SERS activity, and it is the most important parameter in studies on SERS mechanisms. The EF was calculated by randomly selecting 8 points from an Ag/FeS array of 80 W sputtering power using an equation [47]:

$$EF = \frac{I_{SERS}}{I_{bulk}} \times \frac{N_{bulk}}{N_{SERS}} \quad (1)$$

where  $I_{SERS}$  and  $I_{bulk}$  are the SERS intensity of the band at  $1627 \text{ cm}^{-1}$  (assigned to MB adsorbed on the Ag/FeS arrays) and the Raman intensity of the band at  $1618 \text{ cm}^{-1}$  (assigned to solid MB), respectively.  $N_{bulk} = A_{laser}hcN_A$ , where  $N_{bulk}$  is the number of molecules in the solid material under illumination,  $A_{laser}$  is the area of the focused laser spot ( $1 \mu\text{m}$  in diameter) for Raman scanning, the confocal depth ( $h$ ) of the Renishaw Micro-Raman spectrometer with  $514 \text{ nm}$  laser excitation is  $19 \mu\text{m}$ ,  $C$  is the density of the MB molecules,  $N_A$  is Avogadro’s constant, and  $N_{SERS}$  is the average number of adsorbed molecules in the scattering volume for the SERS experiments.  $N_{SERS} = A_{laser}N_dA_N/\delta$ , where  $N_d$  is the number density of 200-nm PS,  $A_N$  is the half surface area of one 200-nm PS, and  $\delta$  is the surface area occupied by a single molecule of MB adsorbed on the substrate, which is estimated to be  $0.75 \text{ nm}^2$ .  $N_{bulk}/N_{SERS}$  can be calculated to be  $6.9 \times 10^5$ . Therefore, EF of the cosputtered Ag/FeS arrays can be calculated to be  $1.8 \times 10^6$ . Thus, the SERS effect of the prepared Ag/FeS array substrate shows that the substrate has a good Raman enhancement effect, and the enhancement factor is as high as  $1.8 \times 10^6$ . The substrate prepared by this method has potential value in studies on SERS.

### 3. Materials and Methods

#### 3.1. Chemicals and Materials

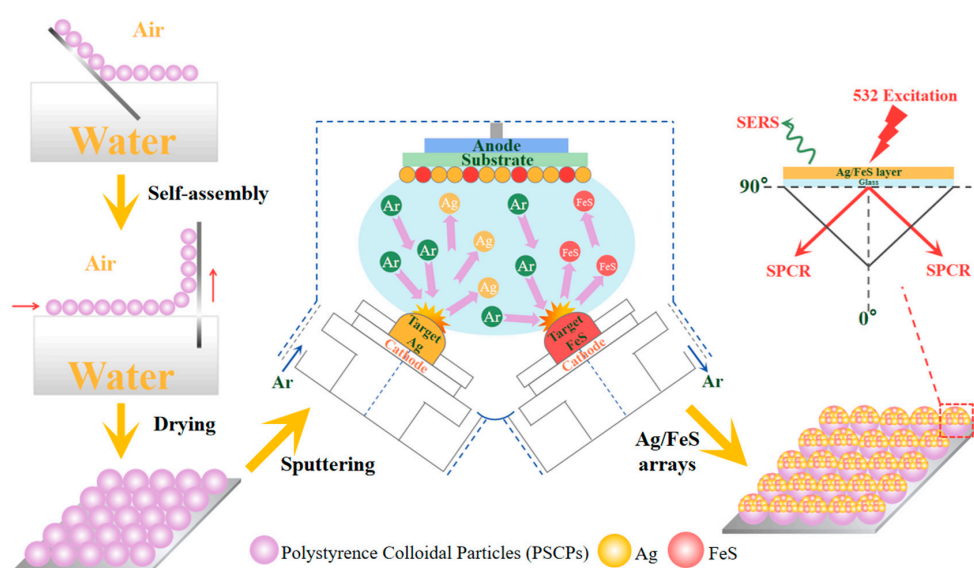
P-type Si (100) wafers with a size of  $200 \mu\text{m}$  were obtained from Hefei Kejing Materials Technology Co., Ltd. (Hefei, China) Monodisperse polystyrene colloidal particles (PSCPs) ( $200 \text{ nm}$ ,  $10 \text{ wt}\%$  aqueous solution) were purchased from Bangs Laboratories Inc. (Shenzhen, China). Sodium dodecyl sulphate (SDS) and methylene blue (MB) were purchased from Sigma-Aldrich Co., Ltd. (Shanghai, China).  $\text{NH}_4\text{OH}$  (25%) and  $\text{H}_2\text{O}_2$  (30%) were purchased from Sinopharm Chemical Reagent Co., Ltd. (Shanghai, China). Ag and FeS targets with purities of 99.99% were obtained from Beijing Tianrui Technology Co., Ltd. (Beijing, China). All chemicals were used without further purification. Ethanol and deionized ultrapure water ( $18.25 \text{ M}\Omega \text{ cm}^{-1}$ ) were used throughout the study.

#### 3.2. Preparation of Two-Dimensional (2D) Ordered PSCP Templates

We prepared two-dimensional (2D) ordered 200-nm PSCP templates by a self-assembly technique. Si wafers (with dimensions of  $2.0 \times 2.0 \text{ cm}$ ) were immersed in a mixture of  $\text{NH}_4\text{OH}$ ,  $\text{H}_2\text{O}_2$  and  $\text{H}_2\text{O}$  in a volume ratio of 1:2:6 and heated at  $300 \text{ }^\circ\text{C}$  for 5 min. The wafers were then ultrasonically washed three times with deionized water and ethanol. The treated Si wafers were immersed in sodium lauryl sulphate for 24 h to make the surfaces hydrophilic. Subsequently, ethanol and 200-nm PSCPs were uniformly mixed at a 1:1 volume ratio and dropped on a large piece of Si wafer. The Si wafer was immersed in water at a tilt angle of  $45^\circ$  and the arrays on the Si wafer were transferred onto the surface of the water. A drop of sodium lauryl sulphate solution was then added to the surface and the PSCPs formed ordered monolayer films on the surface of the water. Finally, the arrays were removed by washing the Si wafer and completely dried in air by static natural evaporation. Tightly packed monolayer ordered arrays were formed on the surface of the Si substrate and stored at room temperature for further use.

### 3.3. Fabrication of Ag/FeS Arrays on PSCP Templates

The FeS and Ag targets were simultaneously deposited onto the 200-nm PSCP templates by a magnetron sputtering system (ATC 1800-F, AJA, North Scituate, MA, USA). The processed Si wafers with the PSCP templates were loaded into the cavity of the magnetron sputtering system; the Ag target and the FeS target were loaded into the magnetic target and the nonmagnetic target, respectively. The target angle was  $10^\circ$  and the distance between the substrate and the target was 20 cm. Then, the main magnetron sputtering chamber was evacuated and the background pressure was lower than  $1.0 \times 10^{-6}$  mTorr when starting the experiment. The Ar gas flow rate was 8.7 sccm (standard cubic centimetres per minute) and the working pressure was on the order of  $5.6 \times 10^{-3}$  mTorr. The sputtering power of Ag was fixed at 5 W during the cosputtering process, the FeS particle size was adjusted by changing the sputtering power of FeS (50, 60, 70, 80 and 90 W) and the sputtering time was 300 s. A schematic of the preparation process of PSCP@Ag-FeS is shown in Scheme 1.



**Scheme 1.** A large, hydrophilic silicon wafer with the ethanol/PSCP mixture was immersed in water at a tilt angle of  $45^\circ$  and the arrays on the Si wafer were transferred onto the surface of the water. Then, the arrays were removed by washing the  $2.0 \times 2.0$  cm Si wafer and they were completely dried in air by static natural evaporation. The FeS and Ag targets were simultaneously deposited onto the 200-nm PSCP templates by a magnetron sputtering system. The SERS spectrum of the PSCP@Ag-FeS-MB assemblies was collected using an excitation wavelength of 514 nm.

### 3.4. Characterization and SERS Measurements

To study the microstructure and morphology of the PSCP@Ag-FeS arrays, we obtained images using scanning electron microscopy (SEM, JEOL 6500F) (JEOL, Tokyo, Japan) at an accelerating voltage of 200 kV. UV-Vis absorption spectra of the PSCP@Ag-FeS arrays were recorded on a Shimadzu UV-3600 UV-Vis spectrometer (Shimadzu, Kyoto, Japan). To measure the elemental composition and chemical state of PSCP@Ag-FeS, X-ray photoelectron spectroscopy (XPS) measurements were performed using a Thermo Scientific ESCALAB 250Xi A1440 system (Thermo Fisher Scientific, Waltham, MA, USA) with Al  $K\alpha$  as the X-ray source and the XPS spectra were referenced to carbon (C 1s = 284.6 eV). The Raman spectra were measured utilizing  $Ar^+$  ion laser excitation in a Renishaw Raman System 2000 spectrometer (Renishaw, London, UK) with a confocal microscope. The PSCP@Ag-FeS ordered arrays prepared by the above cosputtering method were immersed in MB solution at a concentration of  $10^{-3}$  mol/L for 3 h and the Raman spectra of the PSCP@Ag-FeS-MB assemblies were acquired at an excitation wavelength of 514 nm. Throughout the experiment, all chemicals were used as received without further purification.

#### 4. Conclusions

In summary, we prepared a SERS-active substrate by combining self-assembly techniques and magnetron cosputtering of Ag-FeS metal-semiconductor composites on a 200-nm PSCP template. Ag-FeS nanocaps with sputtered films of different thicknesses were obtained by changing the sputtering power of FeS while maintaining the same deposition time and Ag sputtering power. The deposition rate of the film increased as the sputtering power of the FeS target increased. During sputter coating, the deposition rate is proportional to the rate at which atoms escape from the cathode target. In addition, the RF sputtering power is increased, resulting in most of the sputtered particles have high energy and these particles will cause defects at impact points. Since the combined energy of these defective regions is higher than that of the adjacent regions, the defects become the preferred nucleation sites and accelerate film growth and increase the crystallinity of the resulting films. When a large amount of FeS is introduced into the system, the layer will cover the surface of the Ag metal. The coupling between FeS and Ag and the SPR displacement of Ag changes at different sputtering powers, changing the intensity of the SERS spectra, and the enhancement factor is as high as  $1.8 \times 10^6$ . These results clearly demonstrate the high sensitivity of the Ag-FeS nanocap array as a SERS substrate.

**Supplementary Materials:** The following are available online. Figure S1: SEM images of the ordered Ag-FeS arrays at low magnification, which were prepared by cosputtering Ag with a constant sputtering power (5 W) and FeS with varied sputtering powers for 300 s on the PSCP templates. The sputtering powers of FeS were (a) 50 W, (b) 60 W, (c) 70 W, (d) 80 W and (e) 90 W; sputtered pure FeS (f); and pure Ag (g) for 300 s.

**Author Contributions:** N.M. carried out the experiment and wrote the original draft; X.-Y.Z., W.F. and B.H. designed and carried out the experiment; S.J. and Y.P. measured the Raman spectra, L.C. performed the analyses with constructive theoretical discussions; Y.Z., Y.L. and J.Y. revised the manuscript and provided the funding supports; and Y.M.J. revised and edited the whole paper and provided the funding supports. All authors discussed and approved the final version.

**Funding:** This work was supported by the National Natural Science Foundation of China (No. 61575080, 21676115, 51609100 and 21546013), Program for the development of Science and Technology of Jilin province (No. 20160101287J). This work was also supported by the National Research Foundation of Korea (NRF) grant funded by the Korea government (No. NRF-2018R1A2A3074587 and NRF-2017K2A9A2A06014372) and by 2017 Research Grant from Kangwon National University (No. 520170530).

**Acknowledgments:** In this section you can acknowledge any support given which is not covered by the author contribution or funding sections. This may include administrative and technical support or donations in kind (e.g., materials used for experiments).

**Conflicts of Interest:** The authors declare no conflict of interest.

#### References

1. Fleischmann, M.; Hendra, P.J.; Hill, I.R.; Pemble, M.E. Enhanced Raman Spectra from Species Formed by the Coadsorption of Halide Ions and Water Molecules on Silver Electrodes. *J. Electroanal. Chem.* **1981**, *117*, 243–255. [[CrossRef](#)]
2. Dai, Z.G.; Xiao, X.H.; Wu, W.; Zhang, Y.P.; Liao, L.; Guo, S.S.; Ying, J.J.; Shan, C.X.; Sun, M.T.; Jiang, C.Z. Plasmon-driven reaction controlled by the number of graphene layers and localized surface plasmon distribution during optical excitation. *Light Sci. Appl.* **2015**, *4*, e342. [[CrossRef](#)]
3. Rusnati, M.; Sala, D.; Orro, A.; Bugatti, A.; Trombetti, G.; Cichero, E.; Urbinati, C.; Di Somma, M.; Millo, E.; Galletta, L.J.V.; et al. Speeding Up the Identification of Cystic Fibrosis Transmembrane Conductance Regulator-Targeted Drugs: An Approach Based on Bioinformatics Strategies and Surface Plasmon Resonance. *Molecules* **2018**, *23*, 120. [[CrossRef](#)] [[PubMed](#)]
4. Meuser, M.E.; Murphy, M.B.; Rashad, A.A.; Cocklin, S. Kinetic Characterization of Novel HIV-1 Entry Inhibitors: Discovery of a Relationship between Off-Rate and Potency. *Molecules* **2018**, *23*, 1940. [[CrossRef](#)]
5. Schatz, G. Theoretical Studies of Surface Enhanced Raman Scattering. *Acc. Chem. Res.* **1984**, *17*, 370–376. [[CrossRef](#)]
6. Moskovits, M. Surface-enhanced spectroscopy. *Rev. Mod. Phys.* **1985**, *57*, 783–826. [[CrossRef](#)]
7. Adrian, F. Charge transfer effects in surface-enhanced Raman scattering. *J. Chem. Phys.* **1982**, *77*, 5302–5314. [[CrossRef](#)]

8. Lombardi, J.R.; Birke, R.L.; Lu, T.; Xu, J. Charge-transfer theory of surface enhanced Raman spectroscopy: Herzberg-Teller contributions. *J. Chem. Phys.* **1986**, *84*, 4174–4180. [[CrossRef](#)]
9. Hutter, E.; Fendler, J.H. Exploitation of Localized Surface Plasmon Resonance. *Adv. Mater.* **2004**, *16*, 1685–1706. [[CrossRef](#)]
10. Mock, J.J.; Barbic, M.; Smith, D.A.; Schultz, D.A.; Schultz, S. Shape effects in plasmon resonance of individual colloidal silver nanoparticles. *J. Chem. Phys.* **2002**, *116*, 6755–6759. [[CrossRef](#)]
11. Mcfarland, A.D.; Duyn, R.P.V. Single Silver Nanoparticles as Real-Time Optical Sensors with Zeptomole Sensitivity. *Nano Lett.* **2003**, *3*, 1057–1062. [[CrossRef](#)]
12. Kelly, K.L.; Coronado, E.; Zhao, L.L.; Schatz, G.C. The Optical Properties of Metal Nanoparticles: The Influence of Size, Shape, and Dielectric Environment. *J. Phys. Chem. B* **2003**, *107*, 668–677. [[CrossRef](#)]
13. Li, X.; Hu, H.; Li, D.; Shen, Z.; Xiong, Q.; Li, S.; Fan, H.J. Ordered array of gold semishells on TiO<sub>2</sub> spheres: An ultrasensitive and recyclable SERS substrate. *ACS Appl. Mater. Interfaces* **2012**, *4*, 2180–2185. [[CrossRef](#)] [[PubMed](#)]
14. Zhao, Y.; Sun, L.; Xi, M.; Feng, Q.; Jiang, C.; Fong, H. Electrospun TiO<sub>2</sub> nanofelt surface-decorated with Ag nanoparticles as sensitive and UV-cleanable substrate for surface enhanced Raman scattering. *ACS Appl. Mater. Interfaces* **2014**, *6*, 5759–5767. [[CrossRef](#)] [[PubMed](#)]
15. Harraz, F.A.; Ismail, A.A.; Bouzid, H.; Al-Sayari, S.A.; Al-Hajry, A.; Al-Assiri, M.S. Surface-enhanced Raman scattering (SERS)-active substrates from silver plated-porous silicon for detection of crystal violet. *Appl. Surf. Sci.* **2015**, *331*, 241–247. [[CrossRef](#)]
16. Cheng, C.; Yan, B.; Wong, S.M.; Li, X.; Zhou, W.; Yu, T.; Shen, Z.; Yu, H.; Fan, H.J. Fabrication and SERS performance of silver-nanoparticle-decorated Si/ZnO nanotrees in ordered arrays. *ACS Appl. Mater. Interfaces* **2010**, *2*, 1824–1828. [[CrossRef](#)] [[PubMed](#)]
17. Jiang, X.; Li, X.; Jia, X.; Li, G.; Wang, X.; Wang, G.; Li, Z.; Yang, L.; Zhao, B. Surface-Enhanced Raman Scattering from Synergistic Contribution of Metal and Semiconductor in TiO<sub>2</sub>/MBA/Ag(Au) and Ag(Au)/MBA/TiO<sub>2</sub> Assemblies. *J. Phys. Chem. C* **2012**, *116*, 14650–14655. [[CrossRef](#)]
18. Wang, X.; Wang, Y.; Sui, H.; Zhang, X.; Su, H.; Cheng, W.; Han, X.X.; Zhao, B. Investigation of Charge Transfer in Ag/N719/TiO<sub>2</sub> Interface by Surface-Enhanced Raman Spectroscopy. *J. Phys. Chem. C* **2016**, *120*, 13078–13086. [[CrossRef](#)]
19. Zhang, X.; Yu, Z.; Ji, W.; Sui, H.; Cong, Q.; Wang, X.; Zhao, B. Charge-Transfer Effect on Surface-Enhanced Raman Scattering (SERS) in an Ordered Ag NPs/4-Mercaptobenzoic Acid/TiO<sub>2</sub> System. *J. Phys. Chem. C* **2015**, *119*, 22439–22444. [[CrossRef](#)]
20. Otto, A. The ‘chemical’ (electronic) contribution to surface-enhanced Raman scattering. *J. Raman Spectrosc.* **2005**, *36*, 497–509. [[CrossRef](#)]
21. Wang, J.; Lin, W.; Cao, E.; Xu, X.; Liang, W.; Zhang, X. Surface Plasmon Resonance Sensors on Raman and Fluorescence Spectroscopy. *Sensors* **2017**, *17*, 2719. [[CrossRef](#)] [[PubMed](#)]
22. Baffou, G.; Quidant, R. Nanoplasmonics for chemistry. *Chem. Soc. Rev.* **2014**, *43*, 3898–3907. [[CrossRef](#)] [[PubMed](#)]
23. Wu, K.; Chen, J.; McBride, J.R.; Lian, T. Efficient Hot-Electron Transfer by a Plasmon-Induced Interfacial Charge-Transfer Transition. *Science* **2015**, *349*, 632–635. [[CrossRef](#)] [[PubMed](#)]
24. Papa, L.; Freitas, I.C.D.; Geonmonond, R.S.; Aquino, C.B.D.; Pieretti, F.C.; Domingues, S.H.; Ando, R.A.; Camargo, P.H.C. Supports Matter: Unraveling the Role of Charge-Transfer over the Plasmonic Catalytic Activity of Silver Nanoparticles. *J. Mater. Chem. A* **2017**, *5*, 11720–11729. [[CrossRef](#)]
25. Wang, Y.; Yan, C.; Chen, L.; Zhang, Y.; Yang, J. Controllable Charge Transfer in Ag-TiO<sub>2</sub> Composite Structure for SERS Application. *Nanomaterials* **2017**, *7*, 159. [[CrossRef](#)] [[PubMed](#)]
26. Chen, L.; Sun, H.; Zhao, Y.; Gao, R.; Wang, Y.; Liu, Y.; Zhang, Y.; Hua, Z.; Yang, J. Iron layer-dependent surface-enhanced raman scattering of hierarchical nanocap arrays. *Appl. Surf. Sci.* **2017**, *423*, 1124–1133. [[CrossRef](#)]
27. Wang, Y.; Zhao, X.; Gao, W.; Chen, L.; Chen, S.; Wei, M.; Gao, M.; Wang, C.; Zhang, Y.; Yang, J. Au/Ag bimetal nanogap arrays with tunable morphologies for surface-enhanced Raman scattering. *RSC Adv.* **2015**, *5*, 7454–7460. [[CrossRef](#)]
28. Hou, B.H.; Wang, Y.Y.; Guo, J.Z.; Ning, Q.L.; Xi, X.T.; Pang, W.L.; Cao, A.M.; Wang, X.; Zhang, J.P.; Wu, X.L. Pseudocapacitance-boosted ultrafast Na storage in a pie-like FeS@C nanohybrid as an advanced anode material for sodium-ion full batteries. *Nanoscale* **2018**, *10*, 9218–9225. [[CrossRef](#)] [[PubMed](#)]

29. Hu, X.; Meng, G.; Huang, Q.; Xu, W.; Han, F.; Sun, K.; Xu, Q.; Wang, Z. Large-scale homogeneously distributed Ag-NPs with sub-10 nm gaps assembled on a two-layered honeycomb-like TiO<sub>2</sub> film as sensitive and reproducible SERS substrates. *Nanotechnology* **2012**, *23*, 385705. [[CrossRef](#)]
30. Quyen, T.T.B.; Su, W.N.; Chen, K.J.; Pan, C.J.; Rick, J.; Chang, C.C.; Hwang, B.J. Au@SiO<sub>2</sub> core/shell nanoparticle assemblage used for highly sensitive SERS-based determination of glucose and uric acid. *J. Raman Spectrosc.* **2013**, *44*, 1671–1677. [[CrossRef](#)]
31. Li, W.; Liu, P.; Zhao, S.; Zhang, K.; Ma, F.; Liu, X.; Chen, X.; He, D. Microstructural evolution, mechanical properties and strengthening mechanism of TiN/Ni nanocomposite film. *J. Alloys Compd.* **2017**, *691*, 159–164. [[CrossRef](#)]
32. Belov, D.S.; Blinkov, I.V.; Volkhonskii, A.O. The effect of Cu and Ni on the nanostructure and properties of arc-PVD coatings based on titanium nitride. *Surf. Coat. Tech.* **2014**, *260*, 186–197. [[CrossRef](#)]
33. Regent, F.; Musil, J. Magnetron sputtered Cr-Ni-N and Ti-Mo-N films: Comparison of mechanical properties. *Surf. Coat. Tech.* **2001**, *142–144*, 146–151. [[CrossRef](#)]
34. Kumar, M.; Mishra, S.; Mitra, R. Effect of Ar:N<sub>2</sub> ratio on structure and properties of Ni-TiN nanocomposite thin films processed by reactive RF/DC magnetron sputtering. *Surf. Coat. Tech.* **2013**, *228*, 100–114. [[CrossRef](#)]
35. Ganeev, R.; Rysanyanskiy, A.I.; Stepanov, A.L.; Usmanov, T. Saturated absorption and nonlinear refraction of silicate glasses doped with silver nanoparticles at 532 nm. *Opt. Quantum Electron* **2004**, *36*, 949–960. [[CrossRef](#)]
36. Zhang, T.; Sun, Y.; Huang, L.; Li, L.H.; Liu, G.; Zhang, X.; Lyu, X.; Cai, W.; Li, Y. Periodic Porous Alloyed Au-Ag Nanosphere Arrays and Their Highly Sensitive SERS Performance with Good Reproducibility and High Density of Hotspots. *ACS Appl. Mater. Interfaces* **2018**, *10*, 9792–9801. [[CrossRef](#)] [[PubMed](#)]
37. Singh, A.N.; Devnani, H.; Jha, S.; Ingole, P.P. Fermi Level Equilibration of Ag and Au Plasmonic Metal Nanoparticles supported on Graphene Oxide. *Phys. Chem. Chem. Phys.* **2018**, *20*, 26719–26733. [[CrossRef](#)] [[PubMed](#)]
38. Ghodselahi, T.; Neishaboorynejad, T.; Arsalani, S. Fabrication LSPR sensor chip of Ag NPs and their biosensor application based on inter-particle coupling. *Appl. Surf. Sci.* **2015**, *343*, 194–201. [[CrossRef](#)]
39. Li, D.; Sun, Y.; Chen, S.; Yao, J.; Zhang, Y.; Xia, Y.; Yang, D. Highly Porous FeS/Carbon Fibers Derived from Fe-Carrageenan Biomass: High-capacity and Durable Anodes for Sodium-Ion Batteries. *ACS Appl. Mater. Interfaces* **2018**, *10*, 17175–17182. [[CrossRef](#)]
40. Gao, J.; Liu, Y.; Xia, X.; Wang, L.; Dong, W. Fe<sub>1-x</sub>Zn<sub>x</sub>S ternary solid solution as an efficient Fenton-like catalyst for ultrafast degradation of phenol. *J. Hazard. Mater.* **2018**, *353*, 393–400. [[CrossRef](#)]
41. Naujok, R.R.; Duevel, R.V.; Corn, R.M. Fluorescence and Fourier Transform Surface-Enhanced Raman Scattering Measurements of Methylene Blue Adsorbed onto a Sulfur-Modified Gold Electrode. *Langmuir* **1993**, *9*, 1771–1774. [[CrossRef](#)]
42. Ruan, C.; Wang, W.; Gu, B. Single-molecule detection of thionine on aggregated gold nanoparticles by surface enhanced Raman scattering. *J. Raman Spectrosc.* **2007**, *38*, 568–573. [[CrossRef](#)]
43. Hulchineon, K.; Hester, R.E.; Albery, W.J.; Hillman, A.R. Raman Spectroscopic Studies of a Thionine-modified Electrode. *J. Chem. Soc. Faraday Trans.* **1984**, *80*, 2053–2071. [[CrossRef](#)]
44. Niu, Z.; Fang, Y. Surface-enhanced Raman scattering system of sample molecules in silver-modified silver film. *Spectrochim. Acta A* **2007**, *66*, 712–716. [[CrossRef](#)] [[PubMed](#)]
45. Khorasaninejad, M.; Walia, J.; Saini, S.S. Enhanced first-order Raman scattering from arrays of vertical silicon nanowires. *Nanotechnology* **2012**, *23*, 275706. [[CrossRef](#)] [[PubMed](#)]
46. Tian, Z.Q.; Ren, B.; Wu, D.Y. Surface-Enhanced Raman Scattering: From Noble to Transition Metals and from Rough Surfaces to Ordered Nanostructures. *J. Phys. Chem. B* **2002**, *106*, 9463–9483. [[CrossRef](#)]
47. Green, M.; Liu, F.M. SERS Substrates Fabricated by Island Lithography: The Silver/Pyridine System. *J. Phys. Chem. B* **2003**, *107*, 13015–13021. [[CrossRef](#)]

**Sample Availability:** Samples of the compounds are not available from the authors.



© 2019 by the authors. Licensee MDPI, Basel, Switzerland. This article is an open access article distributed under the terms and conditions of the Creative Commons Attribution (CC BY) license (<http://creativecommons.org/licenses/by/4.0/>).